remote sensing

MDPI

Article

Longitudinal Structure in the Altitude of the Sporadic E Observed by COSMIC in Low-Latitudes

Zhendi Liu [1], Qingfeng Li [1,*], Hanxian Fang [1] and Ze Gao [2]

[1] College of Meteorology and Oceanography, National University of Defense Technology, Changsha 410000, China; liuzhendi18@nudt.edu.cn (Z.L.); fanghx@hit.edu.cn (H.F.)
[2] Mailbox 5111, Beijing 100094, China; Gaozenudt@hotmail.com
* Correspondence: lqf123@nudt.edu.cn

Abstract: The longitudinal structure in the altitude of the Sporadic E (Es) was investigated for the first time based on the S4 index provided by the Constellation Observing System for Meteorology, Ionosphere, and Climate (COSMIC) in low latitudes. The longitudinal structure is identified as a symmetrically located wavenumber-4 (WN4) pattern within 30°S–30°N. The WN4 occurs primarily during the daytime at the June solstice and equinoxes, with the largest amplitude at the September equinox and the smallest one at the March equinox. It moves eastward with a speed of ~90°/day. The strongest WN4 appears within 10–20°N and 5–15°S in the Northern and Southern hemispheres, respectively. At the June solstice and the September equinox, the WN4 is stronger in the Northern hemisphere than in the Southern hemisphere, while the situation is reversed at the March equinox. The altitude distribution of the convergence null in the diurnal eastward non-migrating tide with zonal wavenumber-3 (DE3) for the zonal wind is similar to that of the WN4. This and other similar features, such as the seasonal variation, eastward speed, and the symmetrical locations, support the dominant role of the DE3 tide for the formation of the WN4 structure.

Keywords: sporadic E; longitudinal structure; wind shear; non-migrating tide; wavenumber-4 (WN4)

Citation: Liu, Z.; Li, Q.; Fang, H.; Gao, Z. Longitudinal Structure in the Altitude of the Sporadic E Observed by COSMIC in Low-Latitudes. *Remote Sens.* **2021**, *13*, 4714. https://doi.org/10.3390/rs13224714

Academic Editors: Yunbin Yuan and Michael Gorbunov

Received: 6 September 2021
Accepted: 8 November 2021
Published: 21 November 2021

1. Introduction

Sporadic E (Es) layers are thin-layered structures with intense, high electron densities at ~80–120 km altitudes. They can become denser than the normal E layer or even the peak F layer. The large electron density structures and their strong vertical density gradients may seriously affect the radio propagation and navigation systems [1]. Traditionally, Es layers are detected by ground-based instruments including ionosondes, incoherent and coherent scatter radars, and in-situ probes onboard rockets. In the past decades, global navigation satellite system (GNSS) radio occultation (RO) signals have been widely used to investigate Es layers [2–6]. It is widely accepted that the mechanism responsible for the formation of this layer is the wind shear at mid and low latitudes. Rocket and incoherent scatter radar observations have shown that Es layers are caused by the vertical convergence of metallic (monoatomic) ions, such as Fe^+, Mg^+, and Na^+ [7]. As a result, these layers are also reported to be related to the sporadic metal layers [8–10]. Numerous studies have investigated the latitude, altitude, thickness, local time (LT), and seasonal and hemisphere variations of the Es layer and their relations to the wind shear, geomagnetic dip angle, meteor influx, and the tidal and planetary waves [11–13].

Since the neutral winds are dominated by solar tides in the E region [14], the close connection between tides and the Es layer is to be expected. The diurnal, semidiurnal, terdiurnal, and quarterdiurnal signatures in the Es intensity and occurrence rate have been reported by previous papers [15–17]. The relationship is particularly close between tides and the Es altitude, since the Es layer usually descends following the wind shear convergence null (where the ion drift velocity divergence has minimal negative value), which is mainly formed by the tidal wind. Based on measurements from the incoherent

scatter radar (ISR), Mathews [18] showed that diurnal and semidiurnal tides were the main agents that control altitude descent of Es layers. This view was also supported by results in ionogram data [19]. Christakis et al. [17] analyzed the ISR data from Arecibo and found that the descent of Es layers was controlled by diurnal tides at low altitudes and semidiurnal tides at higher altitudes. In addition to diurnal and semidiurnal tides, the terdiurnal tidal signature can also be seen in the height variation of the Es layer [5,15]. Generally, the non-migrating tide, which is generated by the latent heat release in the troposphere and propagating upward [20], can induce the longitudinal structure in the thermospheric and ionospheric parameters [21–28]. However, none of previous works has investigated the non-migrating tidal signature of the Es altitude.

Recently, the WN4 pattern has been observed in the occurrence rate of Es layers over the mid and low latitudes [29]. Niu [30] found some consistencies and inconsistencies between the WN4 pattern and the DE3 tide. He demonstrated that the zonal ion drift factor effect is one cause for the inconsistencies. Liu et al. [29] reported that the WN4 structure for the occurrence rate of Es layers was connected with the DE3 tide in the zonal wind. However, it is still unclear whether the longitudinal structure occurs in the height of Es layers. Therefore, the purpose of this paper is to investigate the longitudinal structure in the altitude of the Es layer. The data used in this work are introduced in Section 2. The general features of the longitudinal structure are described in Section 3. The correlation between the DE3 tide and the longitudinal structure and the effect of the geomagnetic field are discussed in Section 4. The main conclusions are summarized in Section 5.

2. Data

GNSS RO is a widely used remote sensing method to monitor ionospheric weather. The amplitude and phase of the GNSS radio signals are usually used to derive the ionospheric scintillation index, which can represent the occurrence of ionospheric irregularities. The Constellation Observing System for Meteorology, Ionosphere, and Climate (COSMIC) is one of the satellite constellations dedicated to RO missions, which consists of six low earth orbiter micro-satellites [31].

In this work, the scintillation (S4) index provided by the COSMIC RO is employed to identify the Es layer during 2007–2018. The data are available on the COSMIC data analysis and archive center (CDAAC) website (http://cdaac-www.cosmic.ucar.edu/ (accessed on 1 September 2021)). The precise orbit determination (POD) antennas onboard sample the amplitude at the L1 band with a 50 Hz rate and calculate the standard deviation with a 1 Hz rate. Then the S4 index is reconstructed by CDAAC ground processing after these data are downloaded. The procedure of deriving the S4 index can be found in the report of Brahmanandam et al. [32]. To avoid the potential effect of geomagnetic disturbances, S4 index under geomagnetic quiet conditions (Kp $\leq$ 3) are used in the following analysis.

The approach to identify Es layers from the profiles here is the same as that in the report of Liu et al. [29]. An RO profile with a maximum S4 index larger than 0.3 in the height range of 85–125 km could be considered to contain an Es layer. The altitude of the maximum S4 index in the profile is assumed to be the peak height of the Es layer. The height interval is set to 85–125 km because Es layers can hardly be formed below 85 km due to the high ion-neutral collision frequency [7,8] and these layers can appear up to 125 km [5]. This approach has been proven effective by Yue et al. [33,34] and has also been used by Yu et al. [35,36] and Qiu et al. [37]. Arras and Wickert [38] reported a high correlation for Es heights obtained by the S4 index and ionosonde measurements. Thus, although the Es altitude derived from the S4 index here might deviate slightly from the correct height [38], these differences should not influence the general features of the climatology, especially for the longitudinal variations focused on in this paper.

Based on the COSMIC S4 data, a large database is obtained for the analysis of the global behavior of the Es altitude. Figure 1 shows the altitude distribution of Es layers derived from the COSMIC S4 index over the low latitudes in both hemispheres during 2007–2018. The Lat range is taken from 30° S to 30° N. It can be seen from Figure 1 that most

Es layers occur in the height range of 90–115 km, with a maximum number at ~100 km. The peak at ~100 km is due to the combined effects of the altitudinal variations for the metal ions density [5] and the ion-neutral collision frequency [7]. The altitude distribution of the Es layer here generally corresponds well with those from other studies [5,35].

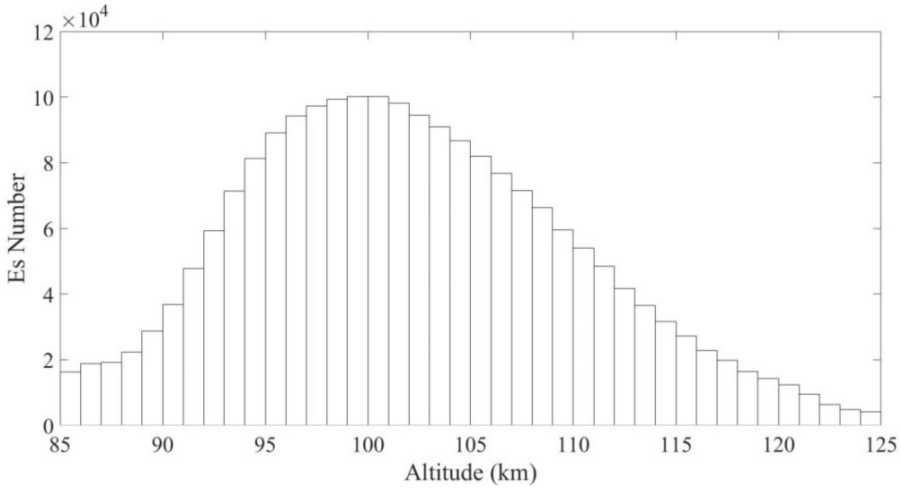

Figure 1. The altitude distribution of the Es layer derived from the COSMIC S4 index over the low latitudes during 2007–2018.

3. Results

Longitudinal structure is such that the height of the Es layer shows zonal difference at a same LT. It can be presented by plotting the global distributions of the averaged Es altitudes in the LT fixed reference. Figure 2 shows such plots for 08–10 LT (the first column), 10–12 LT (the second column), 12–14 LT (the third column), and 14–16 LT (the fourth column) during four seasons denoted by the March equinox (the first row), June solstice (the second row), September equinox (the third row), and the December solstice (the fourth row). Seasons are marked by ±45 days of the equinoxes and solstices. The grid resolution is 5° in geographic longitude (Lon) and 2.5° in geographic latitude (Lat). The solid line in each subfigure depicts the magnetic equator. The most striking feature in Figure 2 is the wave-like structure, which presents four evident peaks over the low latitudes. This longitudinal structure, which is called the WN4 structure, can be identified in both hemispheres at equinoxes and only in the Northern hemisphere at the June solstice. Despite the different intensities, this structure generally locates symmetrically in both hemispheres at equinoxes. It disappears in both hemispheres at the December solstice and instead, a wave-2 like structure occurs.

As shown by Figure 2, the longitudinal structure of the Es height can be identified as the WN4 structure directly from its global distribution during the daytime hours. It is generally located in the low latitudes below 30°. The longitudinal variations of the Es altitude averaged within 0–30° N are presented in Figure 3 at 2 h local time intervals. The results for the March equinox (black lines), June solstice (red lines), and the September equinox (blue lines) are plotted, since the WN4 structure disappears at the December solstice. Note that different scale labels are used for a better visualization, since the Es altitude shows a local time variation. As shown by Figure 3, the WN4 structure becomes visible during 04–06 LT at equinoxes, which is 4 h earlier than the starting time of its occurrence at the June solstice. The WN4 structure persists during the daytime after its appearance around the dawn until it totally vanishes at 20–22 LT. Generally, the WN4 structure shows the largest height difference between crests and troughs at the September equinox, which can be as large as ~6 km at 10–12 LT. The four crests (troughs) are generally separated by ~90° in longitude, and they are located at the similar locations during the three seasons. It is also found that the crests (troughs) move eastward during the daytime. The detailed movement of the crests (troughs) will be described later.

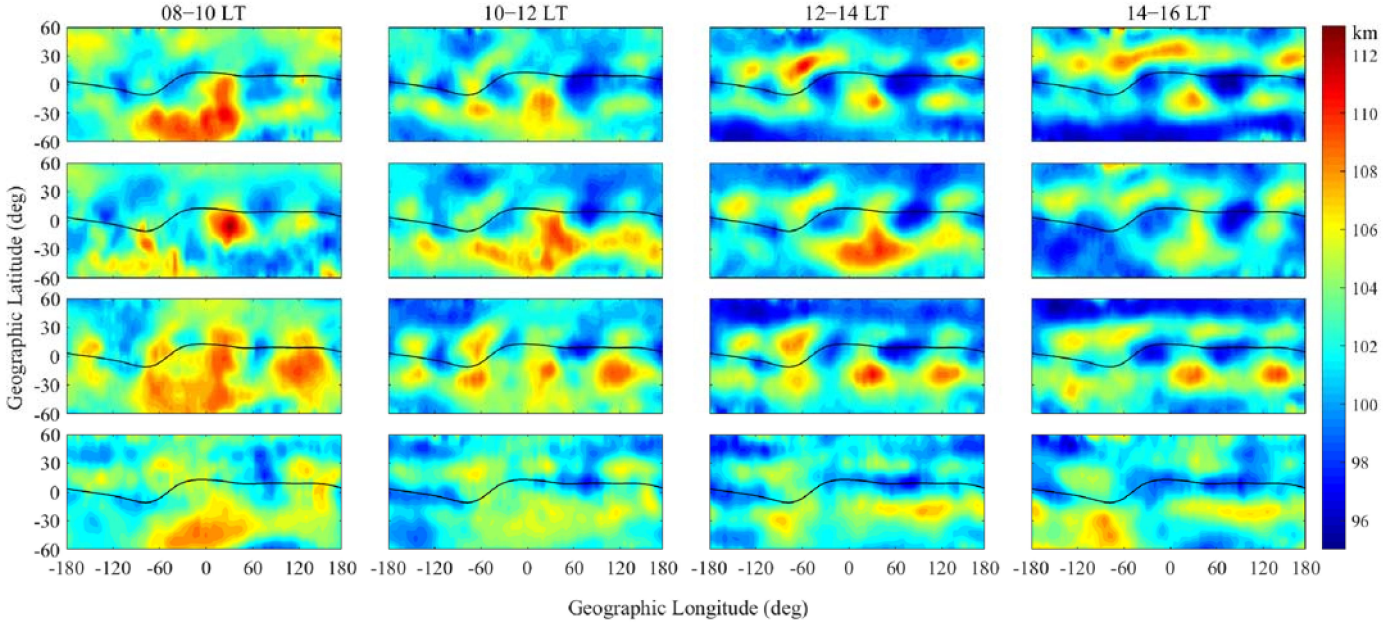

Figure 2. Global distributions of the Es height in the LT fixed reference for the March equinox (**the first row**), June solstice (**the second row**), September equinox (**the third row**), and December solstice (**the fourth row**).

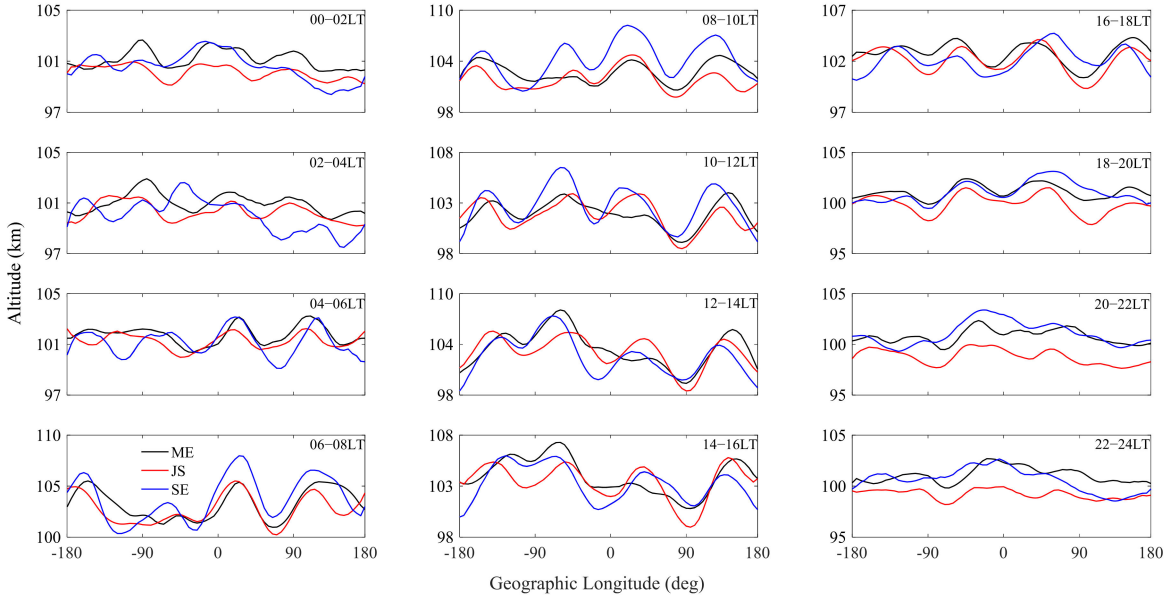

Figure 3. Longitudinal variations of the Es altitude averaged within 0–30° N at the March equinox (black lines), June solstice (red lines), and the September equinox (blue lines).

Similarly, Figure 4 shows the longitudinal variations of the Es altitude averaged within 0–30° S. It is found that the WN4 structure behaves differently at the June solstice. This structure is evident during 06–14 LT, but it is hard to be identified at other times during the day. This different behavior is possibly due to the low occurrence rate of the Es layer in the Southern hemisphere at the June solstice, which will also make it difficult for us to detect the WN4 structure. It also can be seen from Figure 4 that the duration of the WN4 is generally shorter over the Southern hemisphere than over the Northern hemisphere. The starting times for the occurrence of the WN4 over the Southern hemisphere, which are 06–08 LT for the March equinox (08–10 LT for the September equinox), are later than those over the Northern hemisphere. The WN4 structure disappears at 18–20 LT at equinoxes, which is 2 h earlier than that over the Northern hemisphere.

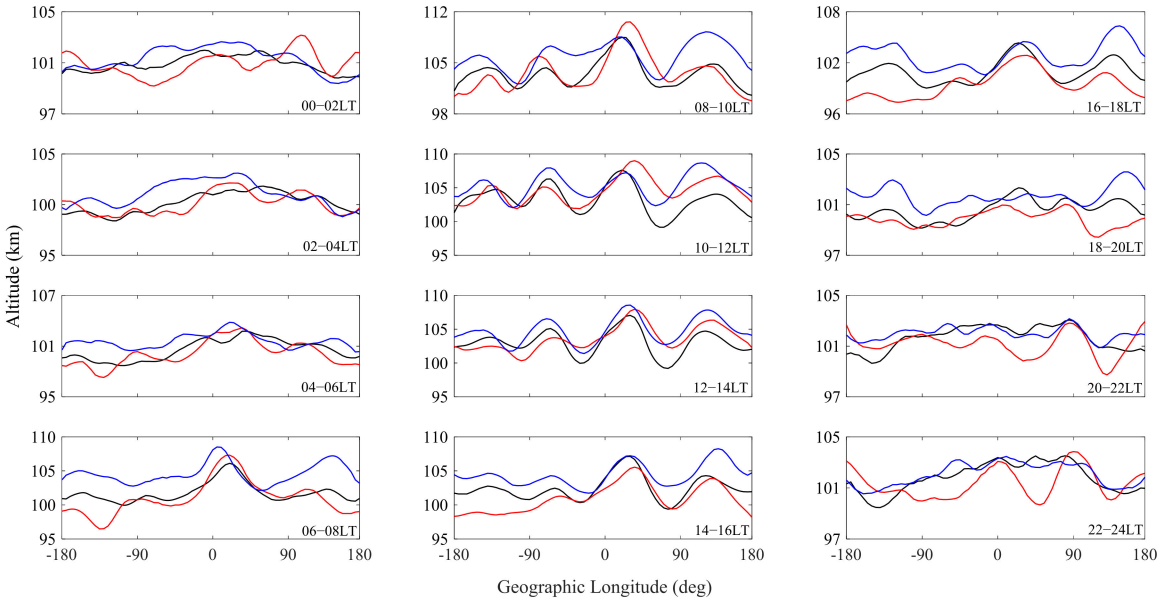

Figure 4. Same as Figure 3, but for 0–30° S.

It was found that the WN4 is the most evident longitudinal structure for the altitude of the Es layer. This structure can be extracted as a component from the measurements by a Fourier transformation (FT) and then an inverse FT. The FT is performed to a series of altitude measurements (H_k) at a longitude series ($Lon_k = 5(k-1)$, $k = 1, 2 \ldots 72$) according to the equation: $A_{W_n} = \frac{p}{72} \cdot \sum_{k=1}^{72} H_k \cdot e^{i \cdot 2\pi n(k-1)/72}$, where $p = \begin{cases} 1, & n = 0 \\ 2, & n > 0 \end{cases}$, $i = \sqrt{-1}$, $n = wavenumber$. The calculated A_{W_4} is the WN4 component.

Figure 5 shows the WN4 components (the right column) picked out from the Es altitudes (the middle column) averaged within 0–30°N. The spectral amplitudes A_{W_n} obtained by the FT are shown in the right column. The eastward shift of the crests is clearly seen in the left column at the equinoxes and the June solstice, although the shift of the second crest (from left to right) is not obvious or even slightly westward at the September equinox. As is seen from the right column, the Es altitude consists of different wave components. The WN4 is the major component in the daytime at the June solstice and September equinox. It is also remarkable in the daytime at the March equinox, although the WN1 structure is stronger than it is in the afternoon. At the December solstice, the WN4 is weak and the WN2 is the main component in the daytime. The dashed lines in the middle column denote a longitude of 90° step within 24 h. The movement of the WN4 component is found to be in general accordance with the dashed line at the equinoxes and the June solstice, which indicates that the average speed of the WN4 pattern is about 90°/day. Another striking feature in the middle column is the seasonal variation of the WN4. It is strong at the June solstice and the September equinox, and relative weak at the March equinox. The similar results for the FT are shown in Figure 6, which are based on the averaged altitude within 0–30°S. Generally, the WN4 shows similar phase distributions in the Southern hemisphere to those in the Northern hemisphere. Some different features are shown by Figure 6. Firstly, the WN4 is relatively weaker at the June solstice than at the equinoxes. As shown by the spectrum, the WN1 is stronger than the WN4 in the daytime at the June solstice. Secondly, there is less consistency between the shift of the WN4 and the dashed line than in the Northern hemisphere, which implies the inconsistency of the eastward movement for the WN4.

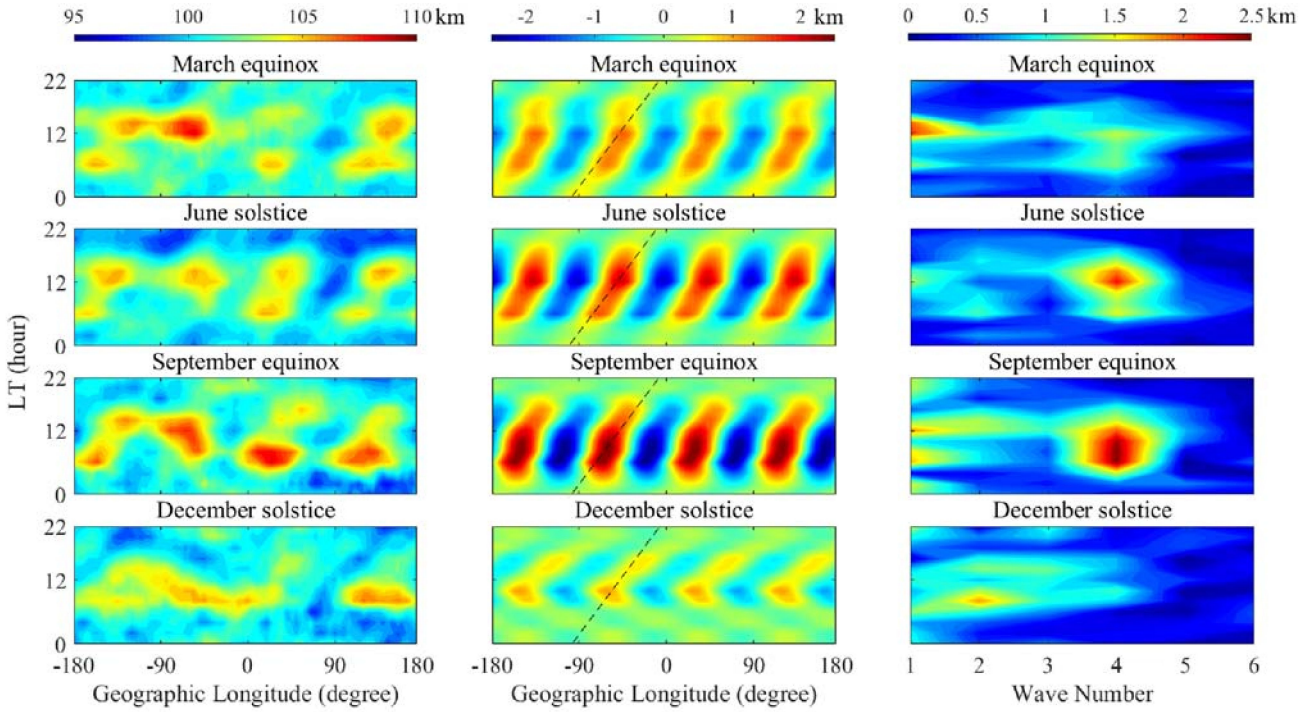

Figure 5. LT-Lon variations of the Es altitude (**the left column**) averaged within 0–30° N and the corresponding WN4 components (**the middle column**), and LT-WN distributions of the amplitude derived from the FT (**the right column**) for the March equinox (**the first row**), June solstice (the second row), September equinox (**the third row**), and December solstice (**the fourth row**). The dashed lines in the middle column denote a longitude of 90° step within 24 h.

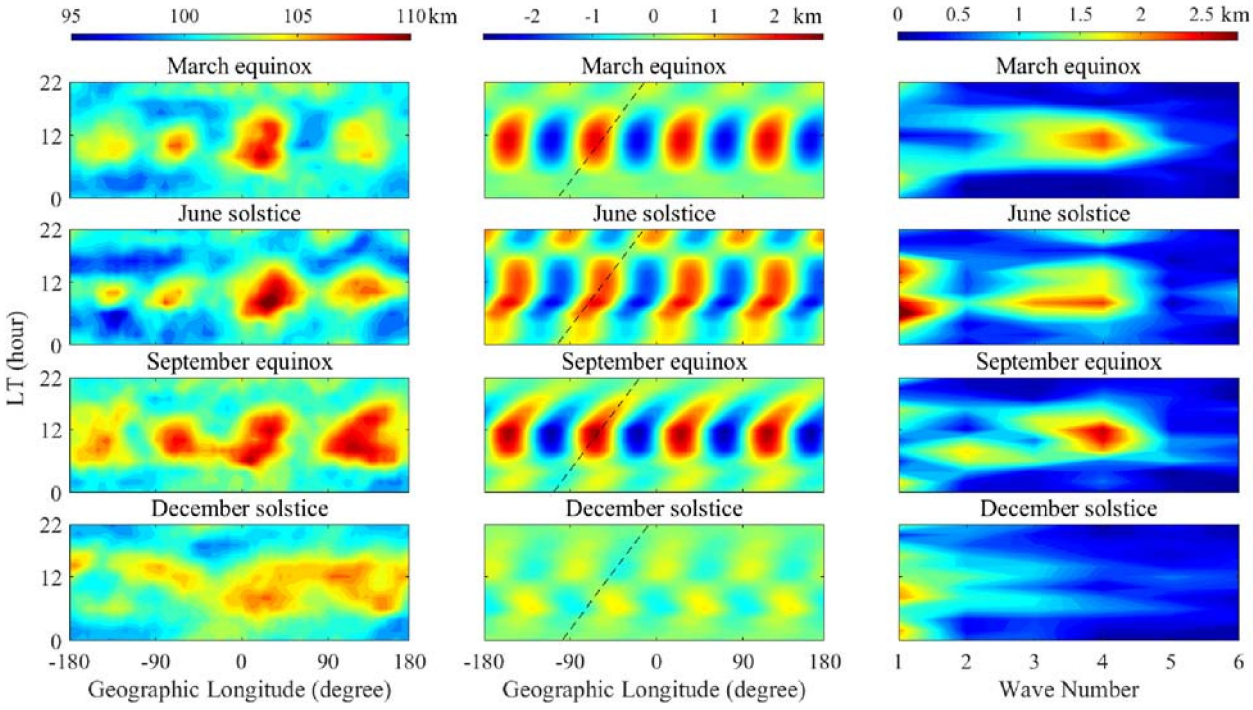

Figure 6. Same as Figure 5, but for 0–30° S.

Figure 7 shows the latitudinal variations of the WN4 structure with 5° intervals within 30°S–30°N for the March equinox (the top row), June solstice (the middle row), and September equinox (the bottom row). The intensity of the WN4 is represented by the amplitude (A_{W_4}) derived from the FT. The seasonal variation presented here is similar to that shown in

Figures 5 and 6. It was found that the WN4 structure generally shows the largest intensity within 10–20°N and 5–15°S in the Northern and Southern hemispheres, respectively. An interesting feature is that the WN4 structure shows asymmetrical intensities in the two hemispheres, although it generally shows symmetrical phases, as shown by Figures 5 and 6. It is easy to understand that the WN4 is stronger in the Northern hemisphere than in the Southern hemisphere at the June solstice, since the Es activity is at a much lower level in the Southern hemisphere at this time. But the asymmetry behaviors seem puzzling at equinoxes. The WN4 structure is stronger in the Southern hemisphere than in the Northern hemisphere at the March equinox, while the situation is reversed at the September equinox.

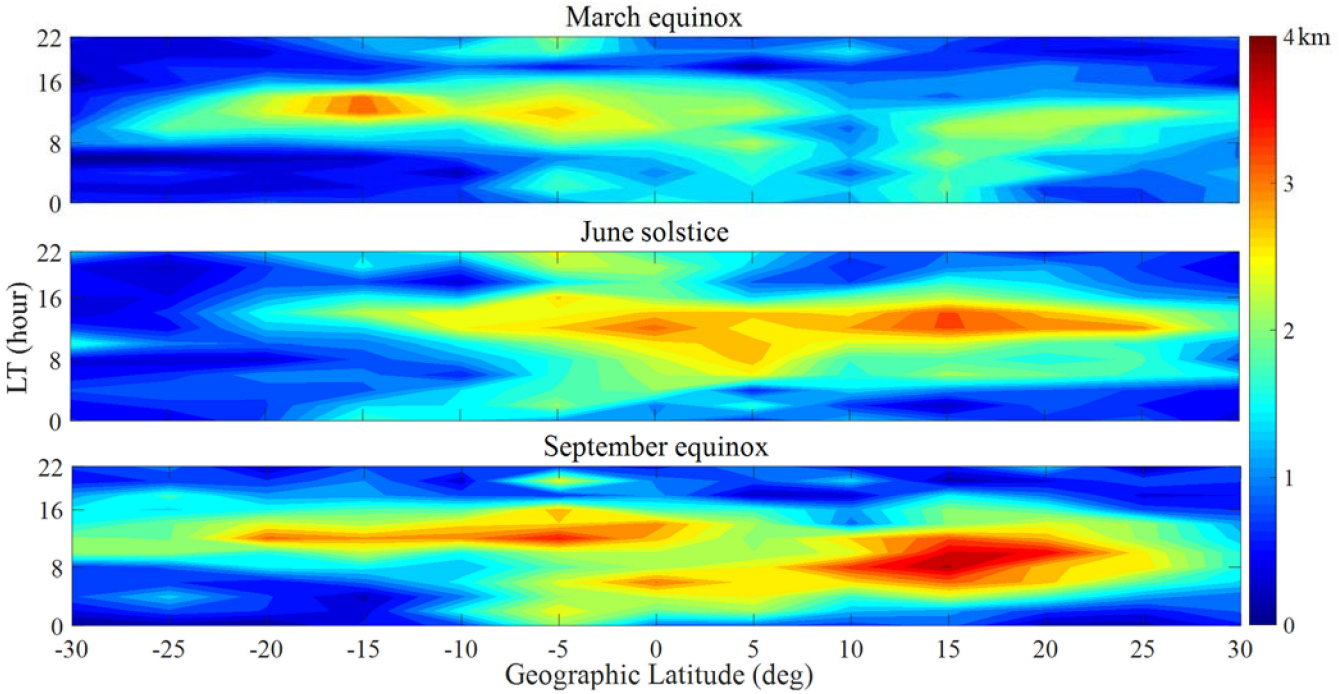

Figure 7. LT-Lat variations of amplitudes derived from the FT for the WN4 component at the March equinox (**the top row**), June solstice (**the middle row**), and September equinox (**the bottom row**).

4. Discussion

In Section 3, the WN4 structure is observed in the global distributions of the Es height; its local time, seasonal, and latitudinal variations are analyzed over the low latitudes. As is known, the WN4 structure has been found in different thermospheric and ionospheric parameters. An observed WN4 structure can be caused by non-migrating tides, including DW5, DE3, SW6, SE2, and SPW4. Oscillations with periods of 24 h and 12 h are referred to as diurnal (D) and semidiurnal (S) tides, respectively. The notation DW*s* and DE*s* are used to describe a westward or eastward propagating diurnal tide with zonal wavenumber *s*. For semidiurnal tides D will be replaced by S. Stationary planetary waves with zonal wavenumber *m* are denoted as SPW*m*. Within 24 h LT, a wave-4 structure caused by DW5 propagates 90° to the west, while DE3 propagates 90° to the east; SW6 displays a phase shift of 180° to the west, while SE2 exhibits 180° to the east; and SPW4 shows no phase shift at all [39]. It is generally accepted that the DE3 tide plays the most important role in the formation of the WN4 structure [20]. As shown in Section 3, the seasonal variation, eastward speed, and the symmetrical distribution of the WN4 are actually similar to those of the DE3 tide.

Using a coordinate system with the x-axis horizontal and towards magnetic north, the y-axis eastward and the z-axis upward, the vertical ion velocity ($w_z(z)$) driven by horizontal winds and the electric field is expressed by the following equation [40]:

$$w_z(z) = \frac{R_i(z)}{1 + R_i^2(z)} \left[\frac{E_z(z)}{B_0(z)} + \frac{\cos I E_y(z)}{B_0(z) R_i(z)} + \cos I U(z) - \frac{\sin I \cos I V(z)}{R_i(z)} \right] \quad (1)$$

where I is the geomagnetic inclination angle, defined as positive (downward) in the Northern Hemisphere; $B_0(z)$ is the total geomagnetic field intensity; $E_y(z)$ and $E_z(z)$ are the zonal and vertical electric fields; $R_i(z)$ is the ratio of the ion-neutral collision frequency ($v_i(z)$) to the ion gyrofrequency (ω_i); U(z) and V(z) are the components of the zonal and meridional neutral winds.

It is widely accepted that the horizontal winds play the dominant role for the formation of the Es layer over the mid-latitudes. The horizontal winds also dominate the Es formation at low latitudes [41–43], although the electric field also has some influence on the formation or disruption process there [44–46]. Therefore, the effect of the electric field is ignored at this stage and will be discussed later. The Es layers will be formed where the vertical divergence of the vertical ion velocity ($\frac{dw_z}{dz}$) reaches the minimal negative value. It can be seen from Equation (1) that the $\frac{dw_z}{dz}$ is controlled by the combined effect of the zonal and meridional wind/windshear, together with the geomagnetic field and the ion-neutral collision frequency. According to the windshear theory, the layer-forming efficiency of the meridional and zonal windshear depends on the height due to the altitude dependences of the ion-neutral collision frequency ($v_i(z)$). At altitudes below ~125 km, where $v_i(z) \gg \omega_i$, the zonal windshear mechanism plays the dominant role [47]. Thus, the WN4 structure for the Es altitude is assumed to be caused by the DE3 tide in the zonal wind through the zonal windshear mechanism. This view will be illustrated hereinafter.

As mentioned above, the Es layers will be formed where $\frac{dw_z}{dz}$ reaches the minimal negative value. It is generally accepted that the vertical divergence of the vertical ion velocity ($\frac{dw_z}{dz}$) is mainly governed by the vertical divergence of the zonal wind velocity over the mid and low latitudes below ~125 km [5,29,48,49]. Therefore, the altitude variation of the Es layer can be represented by the trace of the convergence null, which is defined as the altitude where the tidal wind velocity is zero and the vertical divergence of the tidal wind velocity reaches the minimal negative value (the wind direction is westward above and eastward below this altitude). Figure 8a shows the phase distribution of the DE3 tide in the zonal wind in September. The DE3 tide is provided by the Climatological Tide Model of Thermosphere (CTMT) model. The CTMT is a climatological tidal model, which was developed by Oberheide et al. [50] based on wind and temperature measurements from the thermosphere–ionosphere–mesosphere-energetics and dynamics (TIMED) satellite. As demonstrated in Figure 8a, the phase of the DE3 tide generally shows symmetrical distribution over the Northern and Southern hemispheres in the altitude range of ~95–150 km. In the Northern hemisphere, the altitude range of 80–125 km almost covers a full vertical wavelength of the DE3 tide. Thus, a convergence null will occur in that altitude range at any LT. Figure 8b shows the altitude distribution of the convergence null within that altitude range for the zonal band at 15° N, where the WN4 is very strong, as shown by Figure 7. Note that the height resolution for the CTMT model is 2.5 km, so the result is unsmooth. It can be found that four maximums and four minimums occur in the zonal band at any LT. The maximums and minimums are separated from each other by ~90° in longitude. They move 90° eastward in Lon in 24 h. However, the longitudinal variation of the height for the convergence null is not a wave-like structure due to the sharp gradient between the maximums and the minimums. When compared with the result shown in Figure 5, it was found that the distributions of the maximums are in good accordance with those of the crests in Figure 5, while the distributions of the minimums are quite different from those of the troughs. The consistency between the distribution of the crests for Es altitude WN4 and that of the maximum heights for the convergence null supports

the connection between the WN4 structure and the DE3 tide in the zonal wind. The difference between the troughs in Figure 5 and the minimums in Figure 8b is due to the enhanced ion-neutral collisions at lower altitudes. According to the windshear theory, a layer remains inside a shear convergence null only if it forms rapidly enough compared with the time required for the null to phase-propagate downward a distance equal to the layer's width. The layers form rapidly at higher altitudes, therefore, they tend to "stick" at a wind shear convergence null as it descends with the vertical tidal phase speed, while at lower altitudes the situation changes gradually because ion-neutral collisions become increasingly effective in opposing the ion convergence. Therefore, the layers cannot form rapidly enough to remain in a convergence null. As a result, they lag steadily behind the downward propagating convergence null and descend at a velocity smaller than the vertical tidal phase speed. Finally, the layers will begin to disrupt when they are caught up by a divergent tidal node [7]. According to the simulation performed by Christakis et al. [17], the diurnal tide can bring an ion layer down to ~90 km. Therefore, it is reasonable that the distribution of troughs for the WN4 structure in Figure 5 is inconsistent with that of the minimums in Figure 8b. We only show the result for the zonal band at 15° N as an example, since the phase of the DE3 tide shows the minor latitudinal variation in low latitudes. Additionally, the similar conclusion is expected in the Southern hemisphere, because the phase there shows a similar distribution in the altitude range of ~95–125 km, below which the effect is not important as the ion layers seldom descend down there.

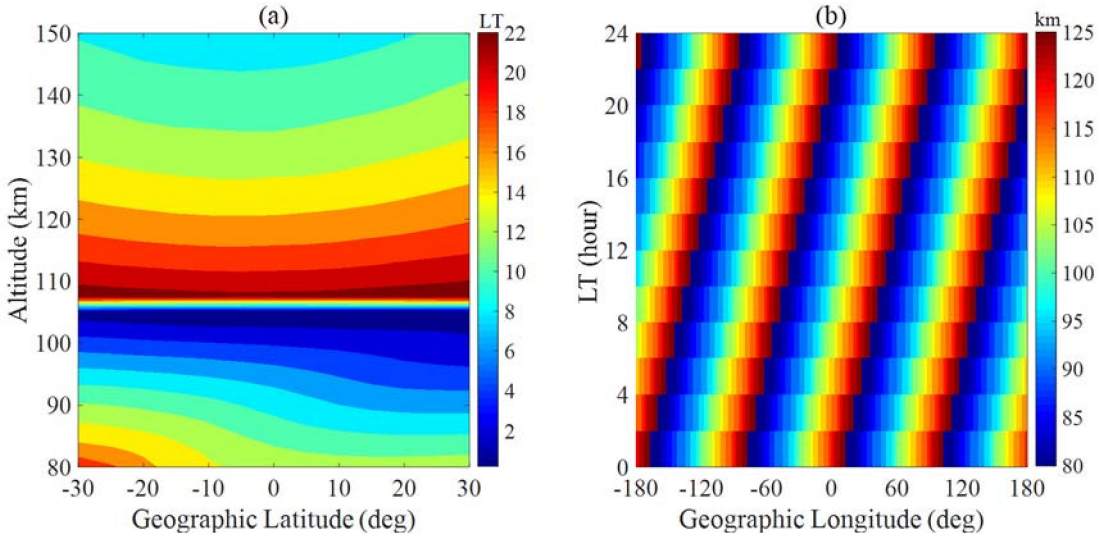

Figure 8. (**a**) The phase distribution of the DE3 tide for the zonal wind in September; (**b**) the altitude distribution of the convergence null for the DE3 tide in the zonal wind in September.

Figure 9 shows the distributions of the amplitudes for the DE3 tide in the zonal wind during different seasons. Similarly, the amplitudes are provided by the CTMT model. As shown, the largest amplitude primarily occurs in the altitude range of 95–115 km, where most Es layers occur. As a result, the WN4 structure becomes a prominent feature in the Es layer. The DE3 tide shows the obvious seasonal variation, with the largest amplitude in September and smallest one in December. This tide is stronger in June than in March. The seasonal variation agrees well with that of the WN4 structure for the Es height, except for the relative weak WN4 at the June solstice in the Southern hemisphere due to the low occurrence rate of the Es layer there. This low occurrence rate is attributed to the interhemispheric transport of metallic ions by the thermospheric meridional circulation [36]. In March, the DE3 is stronger in the Southern hemisphere than in the Northern hemisphere, which agrees well with the asymmetrical distribution of the WN4 structure as shown by Figure 7. The situation changes in September as the amplitude of the DE3 tide generally shows symmetrical distribution, with the peak located slightly southward of the equator

by ~5°. However, the WN4 structure shows a contrary behavior with larger amplitude in the Northern hemisphere. This different behavior needs to be further investigated.

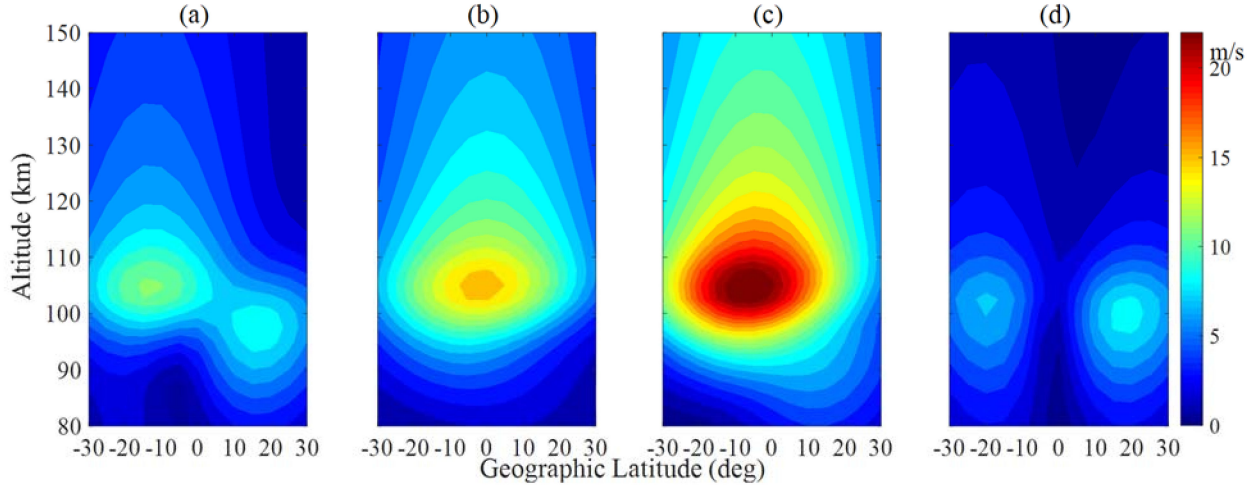

Figure 9. The distributions of the amplitudes for the DE3 tide in the zonal wind during (**a**) March, (**b**) June, (**c**) September, and (**d**) December.

Another interesting feature presented by Figure 9 is the latitudinal distributions during June and September. It was found that the peak amplitude of the DE3 tide occurs in the equatorial region at those times. However, as shown by Figure 7, the strongest WN4 structure occurs in low latitudes but not above the equator, especially for the Northern hemisphere where the strongest WN4 structure is located at ~15° N. This is due to the effect of the configuration of the geomagnetic field, which is another key parameter that controls the Es formation, except the wind. The windshear mechanism fails to work near the magnetic equator, where the geomagnetic field is horizontal, because the ions cannot converge into a layer easily due to the Coulomb force induced by the strongly magnetized electrons. Instead, they are kept near a fixed magnetic field line to maintain plasma neutrality. The windshear mechanism becomes increasingly effective as the geomagnetic inclination angle increases from the equatorial region to the low latitudes. However, the amplitude of the DE3 tide decreases at the same time. Thus, the strongest WN4 structure occurs in the low latitudes. As shown in Figure 2, the WN4 structure also occurs above the magnetic equator, where the Es layer is primarily driven by the electric field [51]. The WN4 there is possibly related to the WN4 structure of the electric field [52].

According to the windshear theory, the electrons are Coulomb-forced to follow the ions in the ion convergence process, moving along the geomagnetic field lines. However, the tides in the neutral wind propagate along the geographic latitude. Thus, the difference between the geomagnetic and geographic latitude may have some influences on the tidal signature in the Es layer. We assume that the inconsistency of the eastward movement for the WN4, as shown by Figure 6 in the Southern hemisphere, is related to the difference between the geomagnetic and geographic latitude. This is due to the offset between the invariant magnetic and the geographic poles being larger in the Southern hemisphere than in the Northern hemisphere [53]. However, this view is incomplete and merits further investigation. Additionally, the chemical process of the metal ions, together with the meteoric ablation and the molecular ions (e.g., NO+ and O_2+), which will control the density of the metal ions [54], may also have an influence on the formation and the variation of the WN4 structure. These factors will be studied in the future through numerical simulation analysis.

It has been reported in some papers that the Es layers do not always occur at the wind shear convergence null [55,56]. Dalakishvili et al. [57] showed that Es layers could also be formed by homogeneous horizontal winds (with no vertical shear). This process is determined by the horizontal wind direction and velocity, geomagnetic field, and ion-neutral

collision frequency and its vertical changes, which can be easily understood according to Equation (1) if we set $\frac{dU}{dz} = \frac{dV}{dz} = 0$. However, this process will not influence the results of climatology in this study. The altitude of the Es layers is treated as a combination of different wave components. The WN4 structure is not the real altitude for Es layers, but is actually the variation of the Es height. Therefore, the dominant role of the DE3 tide is acceptable for the formation of the WN4 structure even though some of Es layers are not formed at the wind shear convergence null.

The WN4 structure is also reported in the occurrence rate of the Es layer by Liu et al. [29]. The structure presented the similar seasonal and latitudinal variations in that work. The WN4 for the occurrence rate in that work aligned with the geomagnetic latitude, while this feature is not evident in this work. This implies that the geomagnetic field has a greater impact on the Es occurrence rate than the Es height. Similarly, the connection was also found between the WN4 of the occurrence rate and the DE3 tide in the zonal wind. However, the process in which the DE3 tide imposes its effect is not the same. The zonal propagation of the DE3 tide is enough for the interpretation of the WN4 in the Es occurrence rate, while the vertical propagation should also be considered when it comes to the WN4 in the Es altitude. This work provides more proof for the correlation between the DE3 tide and the Es layer and demonstrates more comprehensively the effect of the DE3 tide on the Es layer.

5. Conclusions

In this paper, the longitudinal structure in the altitude of the Es layer is investigated for the first time based on the S4 index provided by the COSMIC satellite constellation during 2007—2018. The longitudinal structure is identified as a WN4 pattern within 30°S–30°N. The WN4 primarily occurs at the June solstice and at the equinoxes, with the largest amplitude at the September equinox and the smallest one at the March equinox. It persists during the daytime after its appearance around the dawn until it totally vanishes at ~20LT. The duration of this structure is generally shorter over the Southern hemisphere than over the Northern hemisphere. Generally, this structure shows the symmetrical locations over the two hemispheres with an eastward speed of ~90°/day. The strongest WN4 appears within 10–20°N and 5–15°S in the Northern and Southern hemispheres, respectively. At the June solstice and the September equinox, the WN4 is stronger in the Northern hemisphere than in the Southern hemisphere, while the situation is reversed at the March equinox. The altitude distribution of the convergence null, which is derived from the DE3 tide in the zonal wind based on the CTMT model, is similar to that of the WN4. This and other similar features, such as the seasonal variation, eastward speed, and the symmetrical locations, support the dominant role of the DE3 tide in the zonal wind for the formation of the WN4. This work demonstrates more comprehensively the effect of the DE3 tide on Es layers and could improve our understanding for the formation and variation of these layers.

Author Contributions: Conceptualization, Z.L.; methodology, Z.L.; investigation, Z.L.; resources, Z.L.; data curation, Z.L. and Q.L.; writing—original draft preparation, Z.L., Q.L., H.F., and Z.G.; writing—review and editing, Z.L., H.F., and Z.G.; visualization, Z.L.; supervision, H.F. All authors have read and agreed to the published version of the manuscript.

Funding: This research received no external funding.

Institutional Review Board Statement: Not applicable.

Informed Consent Statement: Not applicable.

Data Availability Statement: The COSMIC S4 index is available at http://cdaac-www.cosmic.ucar.edu/cdaac. The Kp data are available at https://www.spaceweather.gc.ca/solarflux/sx-5-en.php. The CTMT model can be obtained at http://globaldynamics.sites.clemson.edu/articles/ctmt.html. All accessed on 1 September 2021.

Acknowledgments: We acknowledge the University Corporation for Atmospheric Research (UCAR) for providing the COSMIC data. We acknowledge Jens Oberheide for providing the CTMT model. The Natural Resources Canada is also acknowledged for providing the Kp data.

Conflicts of Interest: The authors declare no conflict of interest.

References

1. Pavelyev, A.G.; Liou, Y.A.; Wickert, J.; Schmidt, T.; Liu, S.F. Effects of the ionosphere and solar activity on radio occultation signals: Application to CHAllenging Minisatellite Payload satellite observations. *J. Geophys. Res. Space Phys.* **2007**, *112*, 112. [CrossRef]
2. Wu, D.L.; Ao, C.O.; Hajj, G.A.; de La Torre Juarez, M.; Mannucci, A.J. Sporadic Emorphology from GPS-CHAMP radio occultation. *J. Geophys. Res. Space Phys.* **2005**, *110*. [CrossRef]
3. Arras, C.; Wickert, J.; Beyerle, G.; Heise, S.; Schmidt, T.; Jacobi, C. A global climatology of ionospheric irregularities derived from GPS radio occultation. *Geophys. Res. Lett.* **2008**, *35*. [CrossRef]
4. Chu, Y.H.; Brahmanandam, P.S.; Wang, C.Y.; Su, C.L.; Kuong, R.M. Coordinated sporadic E layer observations made with Chung-Li 30MHz radar, ionosonde and FORMOSAT-3/COSMIC satellites. *J. Atmos. Solar Terr. Phys.* **2011**, *73*, 883–894. [CrossRef]
5. Chu, Y.H.; Wang, C.Y.; Wu, K.H.; Chen, K.T.; Tzeng, K.J.; Su, C.L.; Feng, W.; Plane, J. Morphology of sporadicElayer retrieved from COSMIC GPS radio occultation measurements: Wind shear theory examination. *J. Geophys. Res. Space Phys.* **2014**, *119*, 2117–2136. [CrossRef]
6. Arras, C.; Jacobi, C.; Wickert, J. Semidiurnal tidal signature in sporadic E occurrence rates derived from GPS radio occultation measurements at higher midlatitudes. *Ann. Geophys.* **2009**, *27*, 2555–2563. [CrossRef]
7. Haldoupis, C. A Tutorial Review on Sporadic E Layers. In *Aeronomy of the Earth's Atmosphere and Ionosphere*; Springer International Publishing: Berlin, Germany, 2011; pp. 381–394.
8. Cai, X.; Yuan, T.; Eccles, J.V.; Raizada, S. Investigation on the Distinct Nocturnal Secondary Sodium Layer Behavior Above 95 km in Winter and Summer Over Logan, UT (41.7° N, 112°W) and Arecibo Observatory, PR (18.3° N, 67°W). *J. Geophys. Res. Space Phys.* **2019**, *124*, 9610–9625. [CrossRef]
9. Friedman, J.; Gonzalez, S.A.; Tepley, C.A.; Zhou, Q.; Sulzer, M.P.; Collins, S.C.; Grime, B.W. Simultaneous atomic and ion layer enhancements observed in the mesopause region over Arecibo during the Coqui II Sounding Rocket Campaign. *Geophys. Res. Lett.* **2000**, *27*, 449–452. [CrossRef]
10. Yuan, T.; Wang, J.; Cai, X.; Sojka, J.; Rice, D.; Oberheide, J.; Criddle, N. Investigation of the seasonal and local time variations of the high-altitude sporadic Na layer (Nas) formation and the associated midlatitude descendingElayer (Es) in lowerEregion. *J. Geophys. Res. Space Phys.* **2014**, *119*, 5985–5999. [CrossRef]
11. Haldoupis, C.; Pancheva, D. Planetary waves and midlatitude sporadic E layers: Strong experimental evidence for a close relationship. *J. Geophys. Res. Space Phys.* **2002**, *107*, A6. [CrossRef]
12. Haldoupis, C.; Pancheva, D.; Singer, W.; Meek, C.; Macdougall, J. An explanation for the seasonal dependence of midlatitude sporadic E layers. *J. Geophys. Res. Space Phys.* **2007**, *112*, A6. [CrossRef]
13. Arras, C.; Jacobi, C.; Wickert, J.; Heise, S.; Schmidt, T. Analysis of sporadic E variability derived from GPS radio occultation measurements and possible links to dynamics. In Proceedings of the EGU General Assembly Conference, Vienna, Austria, 21 April 2009.
14. Forbes, J.M.; Zhang, X.; Palo, S.; Russell, J.; Mertens, C.J.; Mlynczak, M. Tidal variability in the ionospheric dynamo region. *J. Geophys. Res. Space Phys.* **2008**, *113*. [CrossRef]
15. Haldoupis, C.; Pancheva, D. Terdiurnal tidelike variability in sporadic E layers. *J. Geophys. Res. Space Phys.* **2006**, *111*, A7. [CrossRef]
16. Haldoupis, C.; Pancheva, D.; Mitchell, N.J. A study of tidal and planetary wave periodicities present in midlatitude sporadic E layers. *J. Geophys. Res. Space Phys.* **2004**, *109*, A2. [CrossRef]
17. Christakis, N.; Haldoupis, C.; Zhou, Q.; Meek, C. Seasonal variability and descent of mid-latitude sporadic E layers at Arecibo. *Ann. Geophys.* **2009**, *27*, 923–931. [CrossRef]
18. Mathews, J. Sporadic E: Current views and recent progress. *J. Atmos. Solar Terr. Phys.* **1998**, *60*, 413–435. [CrossRef]
19. Haldoupis, C.; Meek, C.; Christakis, N.; Pancheva, D.; Bourdillon, A. Ionogram height–time–intensity observations of descending sporadic E layers at mid-latitude. *J. Atmos. Sol. Terr. Phys.* **2006**, *68*, 539–557. [CrossRef]
20. Hagan, M.E.; Forbes, J.M. Migrating and nonmigrating diurnal tides in the middle and upper atmosphere excited by tropospheric latent heat release. *J. Geophys. Res. Space Phys.* **2002**, *107*, D24. [CrossRef]
21. Lühr, H.; Rother, M.; Häusler, K.; Alken, P.; Maus, S. The influence of nonmigrating tides on the longitudinal variation of the equatorial electrojet. *J. Geophys. Res. Space Phys.* **2008**, *113*, A8. [CrossRef]
22. Hartman, W.A.; Heelis, R. Longitudinal variations in the equatorial vertical drift in the topside ionosphere. *J. Geophys. Res. Space Phys.* **2007**, *112*, 112. [CrossRef]
23. Li, G.; Ning, B.; Liu, L.; Zhao, B.; Yue, X.; Su, S.-Y.; Venkatraman, S. Correlative study of plasma bubbles, evening equatorial ionization anomaly, and equatorial prereversalE×Bdrifts at solar maximum. *Radio Sci.* **2008**, *43*. [CrossRef]
24. Wan, W.; Liu, L.; Pi, X.; Zhang, M.-L.; Ning, B.; Xiong, J.; Ding, F. Wavenumber-4 patterns of the total electron content over the low latitude ionosphere. *Geophys. Res. Lett.* **2008**, *35*, 150–152. [CrossRef]

25. Lin, C.H.; Hsiao, C.C.; Liu, J.Y.; Liu, C.H. Longitudinal structure of the equatorial ionosphere: Time evolution of the four-peaked EIA structure. *J. Geophys. Res. Space Phys.* **2007**, *112*, A12. [CrossRef]
26. Liu, Z.; Fang, H.; Hoque, M.M.; Weng, L.; Yang, S.; Gao, Z. A New Empirical Model of NmF2 Based on CHAMP, GRACE, and COSMIC Radio Occultation. *Remote Sens.* **2019**, *11*, 1386. [CrossRef]
27. Oberheide, J.; Forbes, J.M. Thermospheric nitric oxide variability induced by nonmigrating tides. *Geophys. Res. Lett.* **2008**, *35*, 35. [CrossRef]
28. Häusler, K.; Lühr, H.; Rentz, S.; Köhler, W. A statistical analysis of longitudinal dependences of upper thermospheric zonal winds at dip equator latitudes derived from CHAMP. *J. Atmos. Solar Terr. Phys.* **2007**, *69*, 1419–1430. [CrossRef]
29. Liu, Z.; Fang, H.; Yue, X.; Lyu, H. Wavenumber-4 Patterns of the Sporadic E Over the Middle- and Low-Latitudes. *J. Geophys. Res. Space Phys.* **2021**, *126*, 029238. [CrossRef]
30. Niu, J. Relationship Between Wavenumber 4 Pattern of Sporadic E Layer Intensity and Eastward Propagating Diurnal Tide With Zonal Wavenumber 3 in Low Latitude Region. *J. Geophys. Res. Space Phys.* **2021**, *126*, 028985. [CrossRef]
31. Schreiner, W.; Rocken, C.; Sokolovskiy, S.; Syndergaard, S.; Hunt, D. Estimates of the precision of GPS radio occultations from the COSMIC/FORMOSAT-3 mission. *Geophys. Res. Lett.* **2007**, *34*, 545–559. [CrossRef]
32. Brahmanandam, P.S.; Uma, G.; Liu, J.Y.; Chu, Y.H.; Devi, N.S.M.P.L.; Kakinami, Y. Global S4 index variations observed using FORMOSAT-3/COSMIC GPS RO technique during a solar minimum year. *J. Geophys. Res. Space Phys.* **2012**, *117*, A9. [CrossRef]
33. Yue, X.; Schreiner, W.S.; Zeng, Z.; Kuo, Y.-H.; Xue, X. Case study on complex sporadic E layers observed by GPS radio occultations. *Atmos. Meas. Tech.* **2015**, *8*, 225–236. [CrossRef]
34. Yue, X.; Schreiner, W.S.; Pedatella, N.M.; Kuo, Y. Characterizing GPS radio occultation loss of lock due to ionospheric weather. *Space Weather.* **2016**, *14*, 285–299. [CrossRef]
35. Yu, B.; Xue, X.; Yue, X.; Yang, C.; Yu, C.; Dou, X.; Ning, B.; Hu, L. The global climatology of the intensity of the ionospheric sporadic E layer. *Atmos. Chem. Phys. Discuss.* **2019**, *19*, 4139–4151. [CrossRef]
36. Yu, B.; Xue, X.; Scott, C.J.; Wu, J.; Yue, X.; Feng, W.; Chi, Y.; Marsh, D.R.; Liu, H.; Dou, X.; et al. Interhemispheric transport of metallic ions within ionospheric sporadic E layers by the lower thermospheric meridional circulation. *Atmos. Chem. Phys. Discuss.* **2021**, *21*, 4219–4230. [CrossRef]
37. Qiu, L.; Zuo, X.; Yu, T.; Sun, Y.; Qi, Y. Comparison of global morphologies of vertical ion convergence and sporadic E oc-currence rate. *Adv. Space Res.* **2019**, *63*, 3606–3611. [CrossRef]
38. Arras, C.; Wickert, J. Estimation of ionospheric sporadic E intensities from GPS radio occultation measurements. *J. Atmos. Solar Terr. Phys.* **2018**, *171*, 60–63. [CrossRef]
39. Häusler, K.; Luhr, H. Nonmigrating tidal signals in the upper thermospheric zonal wind at equatorial latitudes as observed by CHAMP. *Ann. Geophys.* **2009**, *27*, 2643–2652. [CrossRef]
40. Abdu, M.A.; Macdougall, J.W.; Batista, I.S.; Sobral, J.H.A.; Jayachandran, P.T. Equatorial evening prereversal electric field enhancement and sporadic E layer disruption: A manifestation of E and F region coupling. *J. Geophys. Res. Space Phys.* **2003**, *108*, A6. [CrossRef]
41. Resende, L.C.A.; Batista, I.S.; Denardini, C.M.; Batista, P.; Carrasco, A.J.; Andrioli, V.F.; Moro, J. The influence of tidal winds in the formation of blanketing sporadic e-layer over equatorial Brazilian region. *J. Atmos. Solar Terr. Phys.* **2018**, *171*, 64–71. [CrossRef]
42. Resende, L.C.A.; Arras, C.; Batista, I.S.; Denardini, C.M.; Bertollotto, T.O.; Moro, J. Study of sporadic E layers based on GPS radio occultation measurements and digisonde data over the Brazilian region. *Ann. Geophys.* **2018**, *36*, 587–593. [CrossRef]
43. Resende, L.C.A.; Batista, I.S.; Denardini, C.M.; Batista, P.; Carrasco, A.J.; Andrioli, V.D.F.; Moro, J. Simulations of blanketing sporadic E-layer over the Brazilian sector driven by tidal winds. *J. Atmos. Solar Terr. Phys.* **2017**, *154*, 104–114. [CrossRef]
44. Carrasco, A.J.; Batista, I.S.; Abdu, M.A. Simulation of the sporadic E layer response to prereversal associated evening vertical electric field enhancement near dip equator. *J. Geophys. Res.* **2007**, *112*, A6.
45. Cai, X.; Yuan, T.; Eccles, J.V.; Pedatella, N.M.; Xi, X.; Ban, C.; Liu, A.Z. A Numerical Investigation on the Variation of Sodium Ion and Observed Thermospheric Sodium Layer at Cerro Pachón, Chile During Equinox. *J. Geophys. Res. Space Phys.* **2019**, *124*, 10395–10414. [CrossRef]
46. Cai, X.; Yuan, T.; Eccles, J.V. A Numerical Investigation on Tidal and Gravity Wave Contributions to the Summer Time Na Variations in the Midlatitude E Region. *J. Geophys. Res. Space Phys.* **2017**, *122*, 577. [CrossRef]
47. Haldoupis, C.; Shalimov, S. On the altitude dependence and role of zonal and meridional wind shears in the generation of E region metal ion layers. *J. Atmos. Solar Terr. Phys.* **2021**, *214*, 105537. [CrossRef]
48. Shinagawa, H.; Miyoshi, Y.; Jin, H.; Fujiwara, H. Global distribution of neutral wind shear associated with sporadic E layers derived from GAIA. *J. Geophys. Res. Space Phys.* **2017**, *122*, 4450–4465. [CrossRef]
49. Liu, Y.; Zhou, C.; Tang, Q.; Li, Z.; Song, Y.; Qing, H.; Ni, B.; Zhao, Z.; Li, Z. The seasonal distribution of sporadic E layers observed from radio occultation measurements and its relation with wind shear measured by TIMED/TIDI. *Adv. Space Res.* **2018**, *62*, 426–439. [CrossRef]
50. Oberheide, J.; Forbes, J.; Zhang, X.; Bruinsma, S.L. Climatology of upward propagating diurnal and semidiurnal tides in the thermosphere. *J. Geophys. Res. Space Phys.* **2011**, *116*, 116. [CrossRef]
51. Nygrén, T.; Jalonen, L.; Oksman, J.; Turunen, T. The role of electric field and neutral wind direction in the formation of sporadic E-layers. *J. Atmos. Terr. Phys.* **1984**, *46*, 373–381. [CrossRef]

52. Jin, H.; Miyoshi, Y.; Fujiwara, H.; Shinagawa, H. Electrodynamics of the formation of ionospheric wave number 4 longitudinal structure. *J. Geophys. Res. Space Phys.* **2008**, *113*, 113. [CrossRef]
53. Förster, M.; Cnossen, I. Upper atmosphere differences between northern and southern high latitudes: The role of magnetic field asymmetry. *J. Geophys. Res. Space Phys.* **2013**, *118*, 5951–5966. [CrossRef]
54. Plane, J. Atmospheric Chemistry of Meteoric Metals. *Chem. Rev.* **2003**, *103*, 4963–4984. [CrossRef] [PubMed]
55. Bishop, R.L.; Earle, G.D.; Larsen, M.F.; Swenson, C.M.; Carlson, C.G.; Roddy, P.A.; Fish, C.; Bullett, T.W. Sequential observations of the local neutral wind field structure associated with E region plasma layers. *J. Geophys. Res. Space Phys.* **2005**, *110*, 04309. [CrossRef]
56. Yeh, W.-H.; Liu, J.-Y.; Huang, C.-Y.; Chen, S.-P. Explanation of the sporadic-Elayer formation by comparing FORMOSAT-3/COSMIC data with meteor and wind shear information. *J. Geophys. Res. Atmos.* **2014**, *119*, 4568–4579. [CrossRef]
57. Dalakishvili, G.; Didebulidze, G.; Todua, M. Formation of sporadic E (Es) layer by homogeneous and inhomogeneous horizontal winds. *J. Atmos. Solar Terr. Phys.* **2020**, *209*, 105403. [CrossRef]